

The role of outflows in black-hole X-ray binaries

N. D. Kylafis^{1,2} and P. Reig^{2, 1}

¹ University of Crete, Physics Department & Institute of Theoretical and Computational Physics, 70013 Heraklion, Crete, Greece
e-mail: kylafis@physics.uoc.gr

² Institute of Astrophysics, Foundation for Research and Technology-Hellas, 71110 Heraklion, Crete, Greece
e-mail: pau@physics.uoc.gr

ABSTRACT

Context. The hot inner flow in black-hole X-ray binaries (BHBs) is not just a static corona rotating around the black hole, but it must be partially outflowing. It is therefore a mildly relativistic “outflowing corona”. We have developed a model, in which Comptonization takes place in this outflowing corona. In all of our previous work, we assumed a rather high outflow speed of $0.8c$.

Aims. Here, we investigate whether an outflow with a significantly lower speed can also reproduce the observations. Thus, in this work we consider an outflow speed of $0.1c$ or less.

Methods. As in all of our previous work, we compute by Monte Carlo not only the emergent X-ray spectra, but also the time lags that are introduced to the higher-energy photons with respect to the lower-energy ones by multiple scatterings. We also record the angle (with respect to the symmetry axis of the outflow) and the height at which photons escape.

Results. Our results are very similar to those of our previous work, with some small quantitative differences that can be easily explained. We are again able to reproduce quantitatively five observed correlations: a) the time lag as a function of Fourier frequency, b) the time lag as a function of photon energy, c) the time lag as a function of Γ , d) the time lag as a function of the cut-off energy in the spectrum, and e) the long-standing radio – X-ray correlation. All of them with only two parameters, which vary in the same ranges for all the correlations.

Conclusions. Our model does not require a compact, narrow relativistic jet, although its presence does not affect the results. The essential ingredient of our model is the parabolic shape of the Comptonizing corona. The outflow speed plays a minor role. Furthermore, the bottom of the outflow, in the hard state, looks like a “slab” to the incoming soft photons from the disk, and this can explain the observed X-ray polarization, which is along the outflow. In the hard-intermediate state, we predict for GX 339-4 that the polarization will be perpendicular to the outflow.

Key words. accretion, accretion disks – X-ray binaries: black holes – jets – X-ray spectra

1. Introduction

It is typically accepted that the broad picture of black-hole X-ray binaries (BHBs) consists of an accretion flow (a geometrically thin, cool outer disk and a geometrically thick, hot inner flow) and a narrow relativistic jet. The jet emits in the radio and the infrared, and the hot inner flow acts as a corona that up-scatters soft disk photons to produce the hard X-rays.

The energy spectrum is nicely explained in the above picture as follows: a) radio and at least part of the infrared come from the jet, b) optical, ultraviolet, and some soft X-rays come from the accretion disk, and c) hard X-rays come from the corona (for a review see Remillard & McClintock 2006). On the other hand, it is well known that the spectra of BHBs are almost infinitely degenerate, in the sense that if one is granted freedom on the geometry of the source, the selection between thermal and non-thermal electrons, their energy distribution, and the optical depth to electron scattering, almost any observed energy spectrum can be fitted.

For energies above ~ 2 keV, the harder photons are observed to lag with respect to softer ones. These lags have been explained as the result of propagating fluctuations in the hot inner flow (Nowak et al. 1999a; Kotov et al. 2001; Arévalo & Uttley 2006; Uttley et al. 2011; Uttley & Malzac 2023), light-travel times in the outflow (Reig et al. 2003), the result of impulsive bremsstrahlung injection occurring near the outer edge of

the corona (Kroon & Becker 2016), or as the evolution time-scales of magnetic flares produced when magnetic loops inflate and detach from the accretion disc (Poutanen & Fabian 1999). However, the observed correlation of the lags with the photon-number power-law index Γ of the hard X-rays (Kylafis & Reig 2018; Reig et al. 2018) and with the high-energy cutoff E_c (Altamirano & Méndez 2015), suggest a common origin for the hard X-rays and the time lags. Likewise, the fact that the time-lag – Γ correlation is inclination dependent (Reig & Kylafis 2019) is also difficult to explain with the propagating-fluctuations model.

An important fact that has been neglected in the above picture is that the Bernoulli integral of the hot inner flow is positive (Blandford & Begelman 1999). This means that the matter cannot fall into the black hole. Thus, part of the hot inner flow must escape as an outflow to leave the rest with a negative Bernoulli integral. In other words, the hot inner flow is not just a static corona rotating around the black hole, but a wind-like, “outflowing corona”.

We have been promoting the idea that the above outflow from the hot inner flow is the place where the X-ray spectrum is shaped. The reason is the following: the outflow lies above and below the hot inner flow. Thus, soft photons that are up-scattered in the hot inner flow, must, before they escape, traverse the outflow, where they continue the scattering process. Since, after a few scatterings, the photons forget their initial energy, it

is the scattering in the outflow that determines the emergent X-ray spectrum.

This picture has the advantage that it is very simple. All it requires is a parabolic outflow in which Compton up-scattering of soft photons from the accretion disk takes place. No additional mechanism is required for the time lags. They come naturally with the Compton up-scattering. The harder photons are scattered more times than the softer ones, spend more time in the outflow, and therefore come out later than the softer ones. The size of the outflow and its optical depth determine the magnitude of the time lags. Also, the fact that the time lags and the hard X-ray spectrum are produced by the same process (Comptonization), means that it is not surprising that the two are correlated (Reig & Kylafis 2015; Kylafis & Reig 2018). Furthermore, the Comptonized X-ray spectra that come out of the outflow are anisotropic, because of the shape of the outflow (parabolic) and the outflow speed ($v_0 = 0.8c$). The harder photons come out mainly along the outflow (large optical depth) and the softer ones mainly perpendicular to it (smaller optical depth). This, then, naturally explains the inclination dependence of the time-lag – Γ correlation (Reig & Kylafis 2019).

The parabolic outflow also emits radio waves. In fact, the whole spectrum from radio to hard X-rays can be explained in the outflow model (Markoff et al. 2001; Giannios 2005). In addition, since the same electrons do the Compton up-scattering and the radio emission by synchrotron, it is not surprising that the radio flux correlates with the X-ray flux (Corbel et al. 2013; Kylafis et al. 2023).

In our previous works, we used the word jet to refer to the outflow. In the past, anything outflowing was called "jet". This name now appears inappropriate. Our work reveals that a narrow relativistic jet is not required in this picture. There is no problem if it exists, but it is not necessary.

Here, we want to distinguish between the jet in BHXRBS, which is narrow (a few R_g at its base, R_g is the gravitational radius) and relativistic ($v_0 \gtrsim 0.7c$) and the outflow in BHXRBS, which is wind-like, broad ($10 - 10^3 R_g$ at its base), and non relativistic. The outflow speed cannot be lower than the local escape speed, which is $v_{esc}(R)/c = \sqrt{2R_g/R}$, with R the radial distance. This means that the outflow speed $v_0(R)$ is $> 0.45c$ at $R = 10R_g$ and $> 0.045c$ at $R = 10^3 R_g$. Since in our previous work we used $v_0 = 0.8c$, which for a wide outflow (say $10^2 - 10^3 R_g$) implies a huge mass-outflow rate, unless the matter consists of electron-positron pairs (not likely in BHBs), we need to demonstrate that an outflow with significantly lower speed reproduces the above correlations. This is what we demonstrate in the present paper, but with $v(R) = \text{constant} = 0.1c = v_0$ and not a function of R . The reason for this is because we do not know the mass-outflow rate at every radius R , in order to compute the density in the outflow at a given height as a function of radius. Thus, we feel that a demonstrative calculation, with a low constant outflow speed, will suffice. We comment about this in Sect. 2.7 and 3.

A detailed description of our model is given in Appendix A, where we also describe how our Monte Carlo code works. In Sect. 2, we discuss our results, and in Sect. 3 we give a summary and present our conclusions.

2. Results

In the next sections we present the observational results that our model is capable of reproducing. These results are to be compared with those published over the years in Reig et al. (2003), Kylafis et al. (2008), Reig & Kylafis (2015), Kylafis & Reig

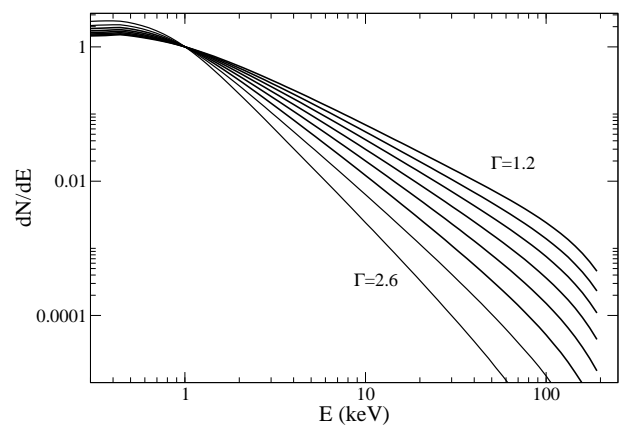


Fig. 1. Energy spectra for different optical depths: from top to bottom $\tau_{\parallel} = 4.5, 4, 3.5, 3, 2.5, 2, 1.5, 1$. The width at the base of the outflow was $R_0 = 400 R_g$ and the Lorentz factor of the coasting electrons was $\gamma_0 = 1.14$. The spectra have been normalized by the flux at 1 keV.

(2018), Reig et al. (2018), Reig & Kylafis (2019), Kylafis et al. (2020), and Reig & Kylafis (2021). Our goal is to demonstrate that a non-relativistic, wind-like outflow (i.e., $v_0 = 0.1c$) can reproduce our previous results (where a mildly relativistic outflow with $v_0 = 0.8c$ was used), which in turn, explain many observations and correlations. In this work, we have assumed that the observer sees the system at an intermediate inclination angle. Hence we combined all the escaping photons with directional cosines in the range $0.2 \leq \cos \theta \leq 0.6$. A full description of the meaning of the model parameters is given in Appendix A.

2.1. Energy spectra

The observed X-ray spectral continuum (0.1–200 keV) of BHBs consists of a soft thermal component and a hard non-thermal component. The thermal component is modeled as a multi-temperature black-body and dominates the spectrum below ~ 2 keV (Mitsuda et al. 1984; Merloni et al. 2000). Its origin is attributed to a geometrically thin, optically thick accretion disk (Shakura & Sunyaev 1973). The non-thermal component is well described by a power law with a high-energy exponential cutoff. This component is believed to be the result of Comptonization of low-energy photons from the accretion disk (Sunyaev & Truemper 1979), by energetic electrons in a configuration that is still under debate.

During X-ray outbursts, BHBs go through different spectral states (McClintock & Remillard 2006; Belloni 2010), of which the two main ones are the soft and hard states (Done et al. 2007). Intermediate states (hard-intermediate, HIMS, and soft-intermediate, SIMS) occur when the source transits from these basic states. Each state is characterized by a different contribution of the thermal and power-law components. In the soft state (SS), the thermal black-body component dominates the energy spectrum, with no or very weak power-law emission (Remillard & McClintock 2006; Dexter & Quataert 2012). In this state the radio emission is quenched. In the hard state (HS), the soft component is weak or absent, whereas the power-law extends to a hundred keV or more with photon-number index Γ in the range 1.2 – 2. In the HIMS, the power-law component is still present, albeit with a steeper slope (i.e., larger Γ) than in the HS, while the black-body component starts to appear (McClintock & Remillard 2006; Castro et al. 2014), if it was not

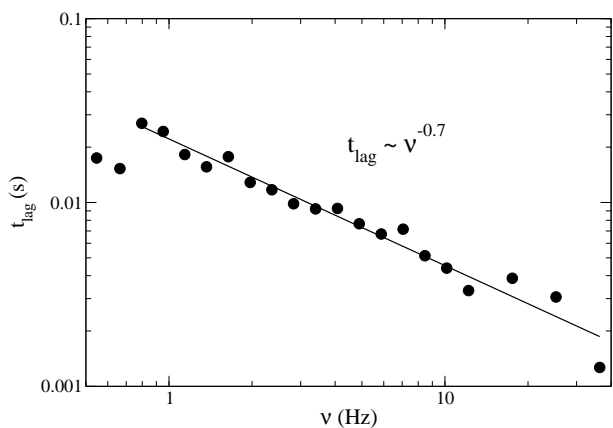


Fig. 2. Time lag as a function of Fourier frequency. The model shown corresponds to $\tau_{\parallel} = 3$, $R_0 = 400 R_g$, and $\gamma_0 = 1.14$.

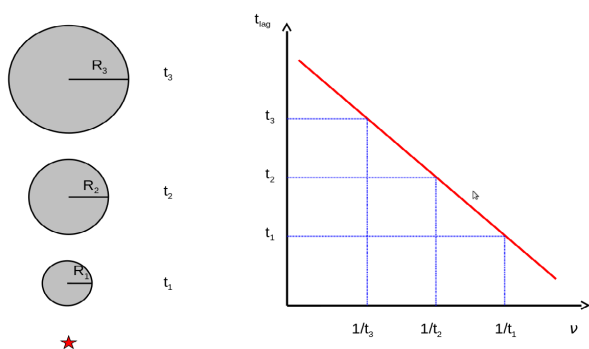


Fig. 3. Explanation of the frequency dependence of time lags.

already there in the HS. In the HS and the HIMS, the systems shine bright in the radio band.

In our model, the Comptonizing medium is the outflow, which extends laterally to relatively large distance (few hundred of R_g at its base) from the black hole. Therefore, our model is relevant for the HS and HIMS and it should be able to reproduce a power-law with photon index in the range 1.2 – 2.6, as measured in the observations.

The main parameter that affects the slope of the continuum is the optical depth τ_{\parallel} (τ_{\perp} is uniquely determined given τ_{\parallel} and R_0), as it is a parameter directly related to the number of scatterings in the outflow. Indeed, we can reproduce the observed range of photon index Γ in the HS and the HIMS by changing the optical depth τ_{\parallel} . Figure 1 shows the resulting energy spectra of our model. Each spectrum corresponds to a model with $R_0 = 400 R_g$, Lorentz $\gamma_0 = 1.14$, and variable τ_{\parallel} between 1 and 4.5, while the rest of the parameters are kept fixed at the reference values given in Table A.1. The spectra have been normalized by the flux at 1 keV. The non-relativistic outflow ($v_0 = 0.1c$) requires lower values of the optical depth to reproduce the photon index of the HS and HIMS, compared to the mildly relativistic outflow that we used before ($v_0 = 0.8c$), for which τ_{\parallel} ranged between 2 and 11 (Reig et al. 2003; Kylafis & Reig 2018).

2.2. Lag-frequency correlation

When two light curves obtained at two separate energy bands (say, a hard and a soft) are cross-correlated, lags are observed between the hard and soft bands. Positive or hard lags mean that the hard photons lag the soft photons. This is always the case

at energies above ~ 2 keV, that is, at energies where the power-law component, typically associated with Comptonization, dominates. The magnitude of this lag strongly depends on Fourier frequency and on the energy bands considered (Miyamoto et al. 1988; Vaughan & Nowak 1997; Cui et al. 1997; Poutanen 2001; Pottschmidt et al. 2003), but typically it is in the range of 1–100 ms. A different type of lags are the so-called reverberation or soft lags, where the soft photons (say, around 0.5 keV) lag the hard ones. These can result from the delay between the hard photons that hit the accretion disk, are absorbed there, and are emitted as soft photons, and the hard photons that reach the observer directly, before the soft photons (Uttley et al. 2014). In this case the soft band is defined at energies below ~ 1 keV, as it comes from the disk (Uttley et al. 2011). Reverberation lags are typically negative, that is, soft photons lag hard photons (Kara et al. 2019). This is explained by the extra path that the absorbed hard X-rays have to travel. In this work we deal with positive lags only.

The positive lags, calculated at energies above ~ 2 keV, can naturally be attributed to inverse Comptonization. In order to acquire their energy, harder photons scatter more times than less hard photons, hence they stay longer in the Comptonizing medium before they escape. In this context, time lags simply signify the difference in light-travel time of photons within the Comptonizing region. A different explanation of the time lags was offered by Lyubarskii (1997, see also Kotov et al. 2001 and Arévalo & Uttley 2006). In this model, the lags result from viscous propagation of mass-accretion fluctuations within the inner regions of the accretion flow.

Observations of time-lags in the hard state show that they roughly follow a power-law dependence on Fourier frequency of the form $t_{\text{lag}} \propto \nu^{-0.8 \pm 0.1}$ (Crary et al. 1998; Nowak et al. 1999b; Cassatella et al. 2012). Our model reproduces quantitatively this nearly $1/\nu$ dependence of the time-lags on Fourier frequency, and this is shown in Fig. 2. The time of flight of all escaping photons was recorded in $N_{\text{bins}} = 8192$ time bins of duration $1/64$ s each. This time was computed by adding up the path lengths traveled by each photon and dividing by the speed of light. Then, we considered the light curves of two energy bands: soft or reference band (2 - 6 keV) and hard (6 - 15 keV). We identified the phase lag ϕ between the signals of the two bands as the phase of the complex cross-vector, and from it the corresponding time lag $\tau = \phi/2\pi\nu$ as a function of Fourier frequency ν .

The black filled circles in Fig. 2 correspond to a model with $\tau_{\parallel} = 3$, $R_0 = 400 R_g$, and $\gamma_0 = 1.14$. The values of these parameters are not crucial, as long as τ_{\parallel} is not too large. The case of large τ_{\parallel} will be explored in a subsequent paper (Reig, Kylafis, & Pe’er, in preparation). It is straight forward to explain qualitatively the above approximately $1/\nu$ dependence of the time-lags, because Compton scattering acts like a filter that cuts off the high frequencies. We explain this below.

For the sake of this argument, let’s think of the outflow as a series of spheres with radii $R_1 < R_2 < R_3 < \dots$, one on top of the other, with the smaller one at the bottom (see Fig. 3). This is a discrete visualization of the parabolic outflow with radius $R(z) = R_0(z/z_0)^{1/2}$, where z_0 is the height above the black hole at which the outflow starts. If τ_{\parallel} is of order unity, then soft photons from the accretion disk, that enter the outflow from below, can scatter in any of the above spheres. The source of soft input photons is indicated in Fig. 3 by a star. Consider soft photons that have an intrinsic variability with period P , i.e., frequency $\nu = 1/P$, and scatter in one of the spheres. If they scatter in the sphere with radius R_1 , this variability will be significantly reduced if the time delay due to Compton scattering, $t_1 = R_1/c$, is

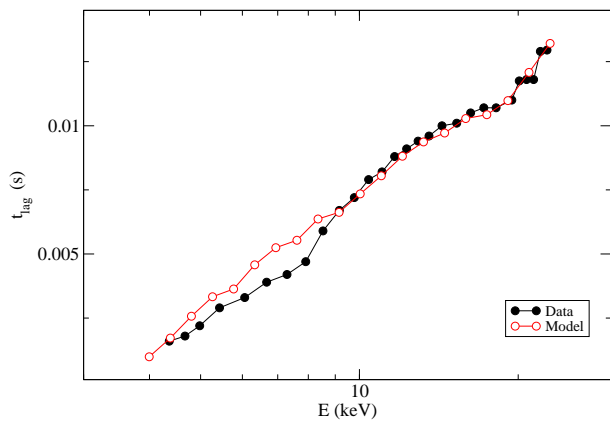


Fig. 4. Lag as a function of energy. Black filled circles represent the observations for Cyg X–1. The model shown as red empty circles corresponds to $\tau_{\parallel} = 2$, $R_0 = 180 R_g$, and $\gamma_0 = 1.14$.

comparable to or larger than P . This means that all frequencies larger than $1/t_1 = c/R_1$ will be essentially washed out. If the scattering occurs in the sphere with radius R_2 , with typical time delay $t_2 = R_2/c$, then all frequencies larger than $1/t_2 = c/R_2$ will be washed out, and so on. In other words, if the time delay due to Compton scattering is t , then all frequencies of variability in the input photons larger than $1/t$ will be washed out. The Monte Carlo Comptonization in a parabolic outflow reproduces the $\nu^{-\alpha}$ dependence, with $\alpha = 0.7 - 0.9$. If the outflow is not parabolic, then Comptonization does not reproduce this frequency dependence. Such outflows will be examined in a subsequent paper and they seem to be related with the outlier sources, i.e., the sources that do not obey the regular radio – X-ray correlation (Gallo et al. 2003; Corbel et al. 2003; Kylafis et al. 2023).

2.3. Lag-energy correlation

In the previous section, we showed that the hard lags observed in the HS of BHBs can be due to the fact that the harder photons have undergone more scatterings inside the outflow (the region where the energetic electrons reside) than lower-energy photons. Also, the energy of the photons changes with every scattering, with an increase in energy, on average. Therefore, both the final amplitude of the lags and the energy with which the photons escape depend on the number of scatterings. Comptonization models predict a log-linear energy dependence in the lags, approximately what is observed (Nowak et al. 1999b; Kotov et al. 2001; Stevens & Uttley 2016). The slope of the relation depends on the range of Fourier frequencies considered to compute the average lag, becoming flatter as the frequency increases (Kotov et al. 2001; Uttley et al. 2011). Observations with good signal-to-noise show that the relation may be more complex than a simple log-linear law, with some bumps or breaks, around the energy of the iron line at 6.4 keV (Kotov et al. 2001; Stevens & Uttley 2016).

Figure 4 shows the energy dependence of the time lag, as computed from our model with $R_0 = 180 R_g$, $\tau_{\parallel} = 2$, and $\gamma_0 = 1.14$. The data are from Kotov et al. (2001) for Cyg X–1. The reference band is 2.7–4 keV and the frequency range of the lag calculation is 0.05–5 Hz, to approximately match the values used by Kotov et al. (2001). In general terms, our model reproduces quite well the approximately linear relation between t_{lag} and $\log E$.

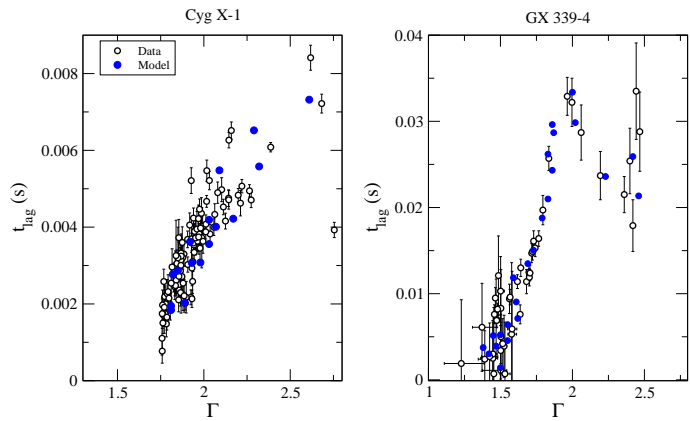


Fig. 5. Correlation between time lag and photon index Γ for Cyg X–1 (left) and GX 339–4 (right). The data for Cyg X–1 come from Pottschmidt et al. (2003, see also Kylafis et al. 2008) and for GX 339–4 from Kylafis & Reig (2018). Black empty circles represent the observations and the filled blue circles correspond to the models, which are produced with $\gamma_0 = 1.14$ and the values of τ_{\parallel} and R_0 that are shown in Fig. 6

2.4. Lag - Γ correlation

Numerous studies have shown that the spectral (e.g., photon index Γ , cutoff energy E_c) and timing (characteristic frequency of the broad-band noise and QPOs, time or phase lags) quantities in BHBs display tight correlations (Di Matteo & Psaltis 1999; Pottschmidt et al. 2003; Kalemci et al. 2003, 2005; Shaposhnikov & Titarchuk 2009; Stiele et al. 2013; Shidatsu et al. 2014; Grinberg et al. 2014; Kalamkar et al. 2015; Altamirano & Méndez 2015; Kylafis & Reig 2018; Reig et al. 2018; Reig & Kylafis 2019; Karpouzias et al. 2021; Méndez et al. 2022). These correlations represent convincing evidence that the timing and spectral properties of the sources are closely linked.

We have demonstrated that our outflow model is able to reproduce the observed correlation between time lag and Γ , not just for a specific source CygX–1 (Kylafis et al. 2008) or GX 339–4 (Kylafis & Reig 2018), but in general for BHBs as a group (Reig et al. 2018). All these correlations were reproduced varying only the optical depth τ_{\parallel} and the width at the base of the outflow R_0 . In those models, the Lorentz factor was $\gamma_0 = 2.24$, which resulted from a high outflow speed $v_0 = 0.8c$ and a moderate perpendicular component $v_{\perp} = 0.4c$. In this work, we show that the outflow speed is not a critical parameter of the model and that a non-relativistic outflow with $v_0 = 0.1c$ can also reproduce the observations. We take $v_{\perp} = 0.47c$, so that $\gamma_0 = 1.14$.

In Fig.5 we show the $t_{\text{lag}} - \Gamma$ correlation for Cyg X–1 (left panel) and for GX 339–4 (right panel). The black empty circles represent the observations and the blue filled circles our models. These figures are to be compared with Fig. 2 in Kylafis et al. (2008) and Fig. 2 in Kylafis & Reig (2018). The energy and frequency ranges used to compute the lags are the same as in the above references, namely between the bands 2–4 keV and 8–14 keV in the frequency range 3.2–10 Hz for Cyg X–1, and between 2–6 keV and 9–15 keV in the 0.05–5 Hz range for GX 339–4. This comparison reveals that even if the outflow speed is reduced from $0.8c$ to $0.1c$, the range of variability of the optical depth τ_{\parallel} and radius R_0 does not change significantly. At the lower outflow speed ($v_0 = 0.1c$), the fits require slightly smaller optical depth and larger radius, $1 \lesssim \tau_{\parallel} \lesssim 6$ and $50 R_g \lesssim R_0 < 1500 R_g$, compared to $2 \lesssim \tau_{\parallel} \lesssim 11$ and $30 R_g \lesssim R_0 \lesssim 600 R_g$ for the $v_0 = 0.8c$ case.

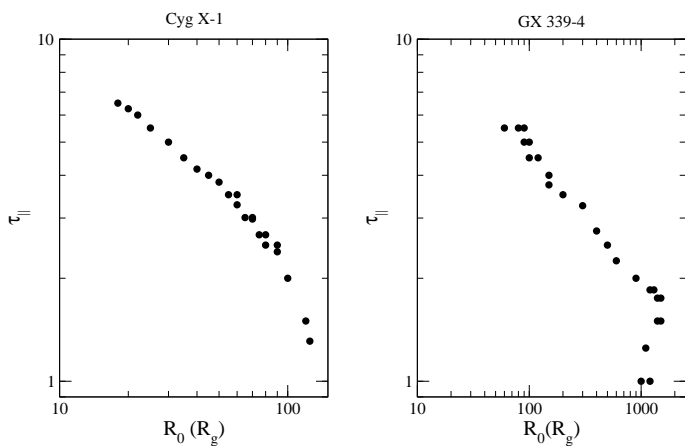


Fig. 6. Correlation between the optical depth τ_{\parallel} and the radius R_0 of the outflow at its base for Cyg X-1 (left) and GX 339-4 (right). The values of the parameters R_0 and τ_{\parallel} are those that were used in the models that produced Fig. 5.

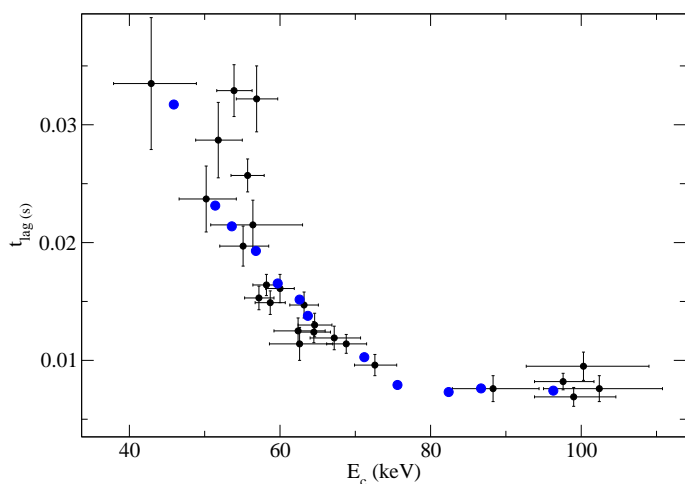


Fig. 7. Relationship between the time lag and cut-off energy. Black circles represent the observations for the BHB GX 339-4. The blue circles correspond to our models. The values of the parameters R_0 and τ_{\parallel} are the same as in the models that were used in Fig. 5.

2.5. τ_{\parallel} - R_0 correlation

One remarkable outcome of our model is the correlation that we have found between the optical depth τ_{\parallel} and the radius R_0 at the base of the outflow (Kylafis et al. 2008; Kylafis & Reig 2018; Reig et al. 2018; Reig & Kylafis 2019). As we mentioned before, we can reproduce a number of observations and correlations by changing only the two basic parameters τ_{\parallel} and R_0 . Surprisingly, these two parameters do not vary independently of one another, but in a correlated manner, following a power law $\tau_{\parallel} \propto R_0^{-\beta}$, in the HS of BHBs. Thus, for the modeling of the HS of BHBs we basically need one parameter, not two. Figure 6 shows this correlation. The points correspond to the models that were used for the explanation of the $t_{\text{lag}} - \Gamma$ correlations shown in Fig. 5. The correlations break down when the source enters the HIMS. The index β is not unique for all BHBs, but different sources display different values of β . For example, for Cyg X-1, $\beta = 0.69$ and for GX 339-4, $\beta = 0.38$. This is to be expected since the amplitudes of the lags of the two sources are significantly different.

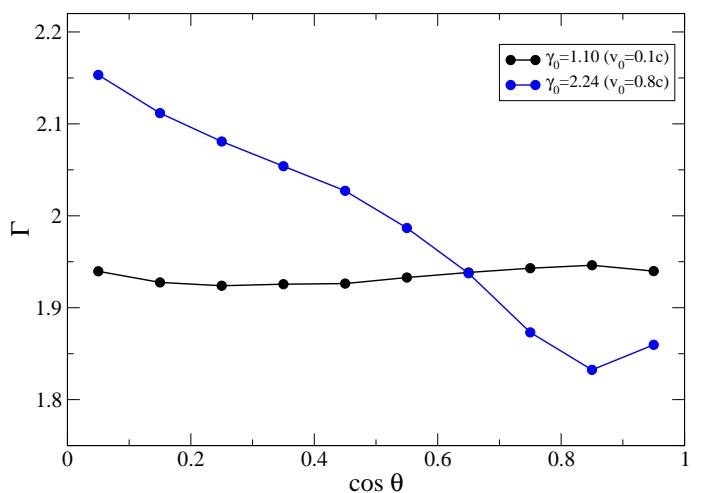


Fig. 8. Photon index as a function of escaping direction. The blue dots are for $v_0 = 0.8c$ and the black dots for $v_0 = 0.1c$. In the inset, we show the corresponding Lorentz γ_0 .

2.6. Lag – cut-off energy correlation

Another interesting result observed in the BHB GX 339-4 is the correlated evolution of the cut-off energy E_c (in its energy spectrum) and the phase-lag ϕ_{lag} of harder photons compared to less hard ones, as the source progresses along the HS (Motta et al. 2009; Altamirano & Méndez 2015). As the X-ray flux increases, the cut-off energy decreases and the amplitude of the time lag increases (see Fig. 7 in Altamirano & Méndez 2015). We showed in Sect. 2.1 that higher optical depths τ_{\parallel} result in harder spectra (the photons are scattered more and gain more energy from the energetic electrons of the outflow). Likewise, by increasing R_0 , the spectrum also hardens, because larger R_0 translates to larger Thomson optical depth τ_{\perp} perpendicular to the axis of the outflow and therefore more scatterings of the photons. For the same reason, the amplitude of the lags increases when the optical depth and/or the radius of the outflow increase. The cut-off energy E_c has a weak dependence on τ_{\parallel} and R_0 , but a rather strong dependence on v_{\perp} . This is because the cut-off is mainly determined by the energetics of the electrons and v_{\perp} determines the maximum energy gain of the soft photons (Giannios et al. 2004; Giannios 2005).

In Reig & Kylafis (2015), we reproduced the correlation between the cut-off energy E_c and the phase lag ϕ_{lag} observed in the BHB GX 339-4 by changing τ_{\parallel} , or v_{\perp} , or both in a correlated way. In that work, we kept R_0 fixed at $100 R_g$. However, as the outburst progresses (i.e., as the X-ray flux increases), we expect that both τ_{\parallel} and R_0 will vary, as we have already shown in Sect. 2.4. Our model requires that as the source moves from the HS to the HIMS, τ_{\parallel} decreases and the R_0 increases.

Here we reproduce again the correlation between lag and cut-off energy in a slightly different form (Fig. 7). We use time lag instead of phase lag and the results of our own analysis instead of data from Motta et al. (2009) and Altamirano & Méndez (2015). The details of the analysis can be found in Reig et al. (2018). We use data from the 2006 outburst of GX 339-4. In Fig. 7, black filled circles represent the observations and blue filled circles the results of our models. We emphasize that the models displayed in Fig. 7 are the same models (i.e., the same combinations of τ_{\parallel} and R_0) that reproduced the $t_{\text{lag}} - \Gamma$ correlation of Fig. 5, simply adjusting slightly the v_{\perp} . The values of v_{\perp} that reproduce the observations vary in the range $0.41c - 0.46c$.

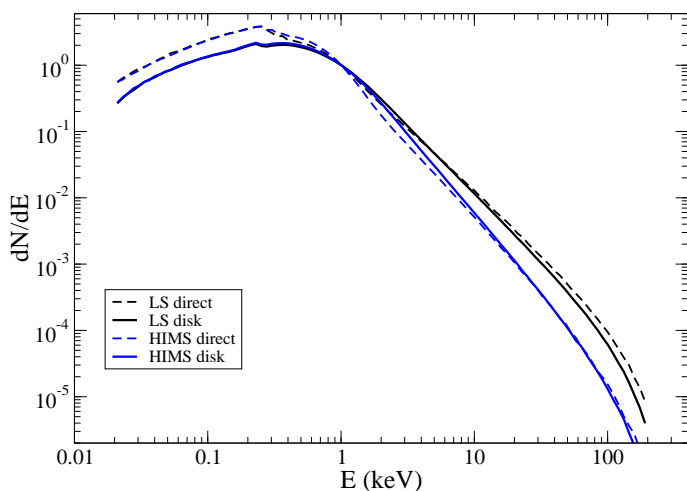


Fig. 9. Comparison of the “direct” and “disk” spectra. The direct spectrum is the spectrum seen by observers at infinity at an inclination $\theta \sim 40^\circ$ and the “disk” spectrum is the spectrum of the photons that are back-scattered and illuminate the disk. The parameters of the models used in this figure for the LS are $\tau_{\parallel} = 2.5$, $R_0 = 500 R_g$, and $\gamma_0 = 1.14$ and for the HIMS $\tau_{\parallel} = 1.5$, $R_0 = 1400 R_g$, and $\gamma_0 = 1.14$.

2.7. Inclination effects

In Reig et al. (2018), we investigated the correlation between t_{lag} and Γ for a large number of BHBs. The data in the correlation showed a large scatter that was explained as an inclination effect (Reig & Kylafis 2019). Systems seen at low inclination exhibit a stronger correlation. In high-inclination systems, the correlation is rather weak. We also showed that low- and intermediate-inclination systems tend to have harder spectra (see also Reig et al. 2003) and a larger amplitude of time lags. The explanation is that, in a mildly relativistic outflow, the high bulk speed of the electrons provides a boost on the photons that makes them scatter preferentially in the forward direction. These photons travel longer distances and suffer more scatterings than photons that escape perpendicularly to the outflow axis. Therefore, photons that escape at small to moderate angles θ with respect to the outflow axis lead to harder spectra (smaller photon index), because they undergo more scatterings and longer lags because they travel longer distances.

Figure 8 shows the dependence of the photon index on the escaping angle for the case of a mildly relativistic outflow with $v_0 = 0.8c$ (blue dots) and a non-relativistic outflow with $v_0 = 0.1c$ (black dots). Here θ is the angle between the observer and the outflow axis (i.e., photons with $\cos \theta \sim 1$ escape along the axis, while $\cos \theta \sim 0$ escape perpendicular to the outflow axis). The parameters of the models shown are $\tau_{\parallel} = 5.5$ and $R_0 = 140 R_g$ for the mildly relativistic outflow and $\tau_{\parallel} = 3.5$ and $R_0 = 150 R_g$ for the non-relativistic outflow.

As we indicated in the Introduction, our model with constant $v_0 = 0.1c$ is only demonstrative because in reality the escape speed is not expected to be constant, but a function of R , and it ranges from $0.58c$ at $R = 6R_g$ to $0.045c$ at $R = 10^3 R_g$. Thus, the real outflow has a central fast part and a progressively slower outer part. Without this variable $v_0(R)$ it is not possible to compute accurately the spectra as a function of inclination.

2.8. Disk illumination

In our model, soft photons are injected isotropically upward at the base of the outflow. Depending on τ_{\parallel} and the initial direction,

photons may escape unscattered or after a number of scatterings. After escape, we record their energy, angle of escape (with respect to the outflow axis), height from the black hole, and travel time in the outflow. Hence, the code also computes the back-scattered photons, i.e., photons with escaping angle $\theta > \pi/2$. Some of these photons will be absorbed by the accretion disk and others will be reflected by it. The code, in its current version, does not account for reflection, but we can measure the number of photons that hit the accretion disk. In other words, we can compute the irradiation spectrum.

In Reig & Kylafis (2021), we showed that the fraction of back-scattered photons increases as the Lorentz factor γ_0 decreases. The reason is that in non relativistic outflows the scattering is nearly isotropic, whereas when the outflow velocity is high, there is a strong forward boost, as explained in the previous section. Although in our model photons can interact with electrons anywhere in the outflow, most of the scatterings occur close to the black hole, not far away from the base of the outflow if the outflow velocity is low.

Fig. 9 compares the energy distribution of the photons that illuminate the disk, that is the “disk” spectrum (solid line), with the “direct” spectrum of the photons from the outflow, seen by observers for typical LS and HIMS spectra. Unlike the relativistic case with $v_0 = 0.8c$, where the “disk” spectrum was much softer than the “direct” one (see Fig. 3 of Reig & Kylafis 2021), here the “disk” and the “direct” spectra are very similar. The spectra, both “direct” and “disk”, are slightly softer in the HIMS than in the LS, in agreement with observations.

Another way to investigate the irradiation of the accretion disk by the primary source is by computing the emissivity profile, which is the radially dependent flux irradiating the disk by the source. For a standard Shakura-Sunyaev accretion disk, it is parameterized as a power law $F(r) \propto r^{-q}$, with q the emissivity index. The standard behavior is $q = 3$ (Dauser et al. 2013). To compute the emissivity index, we divided the accretion disk into radial zones and computed the number of photons per unit area that irradiate a given zone. For the sake of the computation and in order to compare with the lamppost geometry, we collapsed the outflow to $R_0 = 1 R_g$. We find that for $R_{\text{disk}} \gtrsim 10 R_g$, the radial dependence of the irradiated flux on the disk does follow a power-law with $q = 3$, that is, the expected value for a standard Shakura-Sunyaev disk¹.

Fig. 10 shows the distribution of distances h from the black hole from which the photons that hit the accretion disk escape. We show this distribution for different values of τ_{\parallel} (top panel) and R_0 (bottom panel) and two Lorentz factors $\gamma_0 = 1.10$ and $\gamma_0 = 2.24$ (i.e., $v_0 = 0.1c$ and $v_0 = 0.8c$, respectively). As expected, most of the photons escape within a few R_g , but a significant fraction of the photons that hit the accretion disk also escape at tens to few hundreds of R_g . This figure also confirms the fact that disk illumination increases as the outflow speed decreases. The vertical axis in Fig. 10 is reminiscent of the reflection fraction, defined as the number of emitted photons of the primary source which hit the accretion disk N_{AD} over the number of photons escaping to infinity N_{∞} (Dauser et al. 2014, 2016).²

¹ When relativistic effects are taken into account, steeper profiles are found in the inner parts of the accretion disk (Dauser et al. 2022) and a broken power law is used instead (Bambi et al. 2020). We note that because our model deals with broad outflows, relativistic effects are not expected to play any significant role in our results.

² Here we have employed $N_{\text{AD}}/N_{\text{phot}}$, instead of N_{AD}/N_{∞} , where N_{phot} is the total number of photons coming out from the outflowing corona and $N_{\infty} = N_{\text{phot}} - N_{\text{AD}}$.

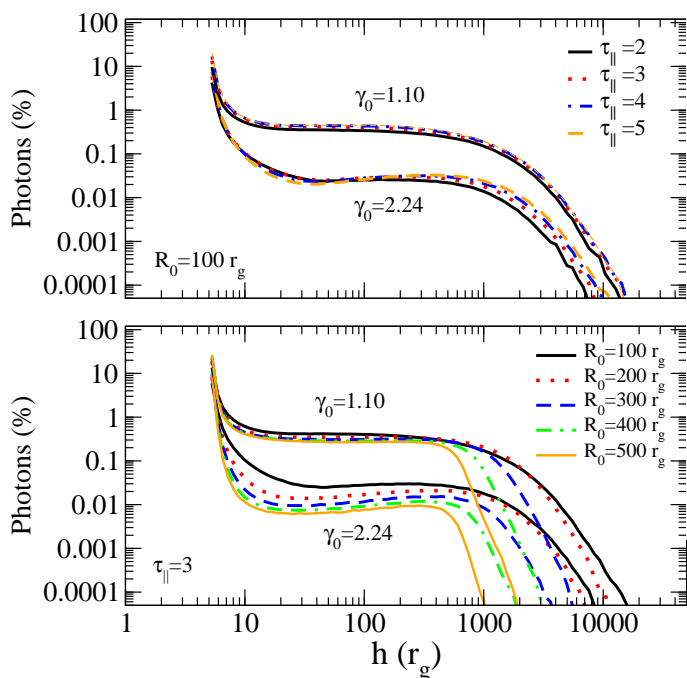


Fig. 10. Fraction of photons that hit the accretion disk over the total number of photons as a function of distance h from the black hole at which they escape, for different values of the optical depth τ_{\parallel} and radius R_0 of the outflow. The distribution is shown for a mildly relativistic

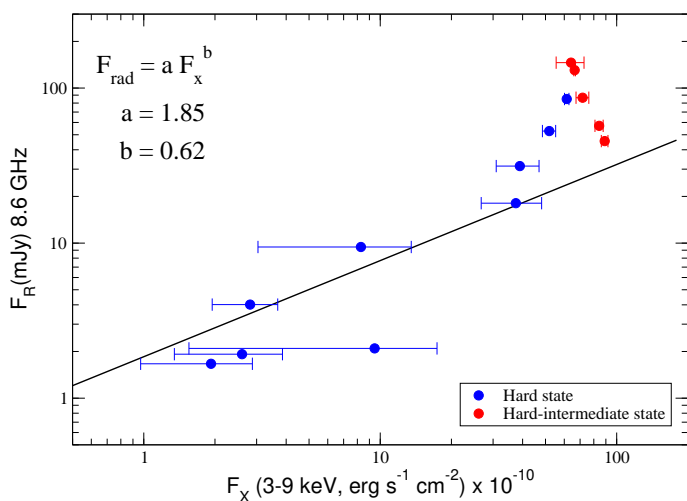


Fig. 11. Radio–X-ray flux correlation for GX 339–4. The models used to compute the radio flux and the theoretical Γ are the same as those that reproduce the time lag– Γ correlation displayed in Fig. 5.

2.9. The radio – X-ray correlation

One of the most tight correlations in BHBs is the radio–X-ray correlation (Hannikainen et al. 1998; Corbel et al. 2000, 2003; Gallo et al. 2003; Bright et al. 2020; Shaw et al. 2021). The correlation extends over five orders of magnitude in radio flux and eight orders of magnitude in X-rays. The radio – X-ray correlation is in the form of a power-law $F_R \propto F_X^\delta$, where $\delta \approx 0.5 - 0.7$ (Gallo et al. 2012; Corbel et al. 2013). In addition to the main correlation, a group of outliers populate the $F_R - F_X$ plane (Gallo et al. 2012). The group of outliers is associated with radio quiet sources, while most of the sources that follow the standard

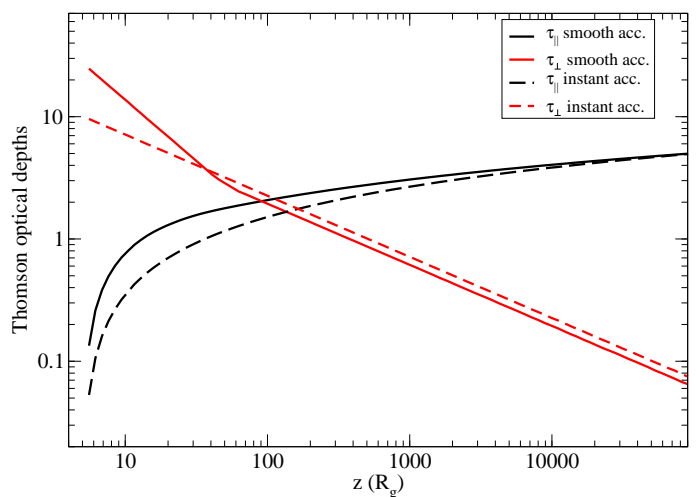


Fig. 12. Thomson optical depths (parallel and perpendicular to the outflow) as functions of distance from the black hole. We show two cases: instant acceleration of the outflow (dashed lines) and when an acceleration region is present, i.e., smooth acceleration (solid lines). We used a model with $\tau_{\parallel} = 5$ and $R_0 = 100 R_g$, where R_g is the gravitational radius.

correlation are radio loud systems (Espinasse & Fender 2018). This difference in radio emission could be an inclination effect (Motta et al. 2018), though other possibilities should be examined. Here we show that our model can reproduce the standard $F_R - F_X$ correlation. In particular, for the best-studied BHB GX 339–4, for which the correlation stands for more than five orders of magnitude in X-ray flux, the exponent is $\delta = 0.62 \pm 0.01$ (Corbel et al. 2013).

We follow the same procedure as in Kylafis et al. (2023), where we reproduced the $F_R - F_X$ correlation for the case of a mildly relativistic outflow, i.e., $v_0 = 0.8c$. From the X-ray observations of the 2007–2008 outburst of GX 339–4, we obtained a relationship between X-ray flux and photon-number spectral index Γ . We rebinned the data in bins of 0.05 in Γ for the HS and 0.1 for the HIMS. The error in the flux was computed as the standard deviation of the data in each bin. From our model, we computed the radio flux and the X-ray spectrum, i.e., the spectral index Γ , for each set of input parameters (R_0, τ_{\parallel}). Thus, we obtained an entirely theoretical relationship between radio flux and photon index Γ . We stress that our model input parameters are not arbitrary, but they are exactly the same as those in Fig. 6 (right panel), which reproduce the correlation between time lag and Γ , shown in Fig. 5 (right panel). Thus, we attempt to explain two correlations with the same model parameters.

From the observed $F_X - \Gamma$ correlation and the computed $F_R - \Gamma$ one, we matched the radio and X-ray fluxes that have the same or very similar value of Γ , and plotted one against the other. The result is shown in Fig. 11. We refer the reader to Appendix A (see also Giannios 2005; Kylafis et al. 2023) for the computation of the radio flux with our model as well as the details of the analysis of the X-ray observations. The black line Fig. 11 is not a fit to the blue dots, but it is the observational correlation of (Corbel et al. 2013). The blue dots correspond to the HS and the red dots to the HIMS. The only quantity that we had to change in this calculation, as compared with the one reported in Kylafis et al. (2023), is the magnetic field B_0 at the base of the outflow. Here, its value is 2.9×10^4 G.

2.10. X-ray polarization

Recent results from the Imager X-ray Polarimetry Explorer (IXPE) mission (Weisskopf et al. 2022) have revealed that BHs show polarization degrees in the X-ray band (2–8 keV) of a few percent and the polarization angle is aligned with the outflow (Krawczynski et al. 2022; Veledina et al. 2023; Ingram et al. 2023; Rodriguez Cavero et al. 2023). Since Comptonization in a slab (with Thomson optical depth in the plane of the slab much larger than in the perpendicular direction) gives rise to linear polarization perpendicular to the slab (Poutanen et al. 1996; Schnittman & Krolik 2010), people typically assume the Comptonizing corona to be in the form of a slab, perpendicular to the outflow, but without giving a physical justification for this. Also, models with a static Comptonizing region predict a lower polarization degree than the observed one. One way to produce higher polarization is by assuming that the inner disk is viewed at a higher inclination angle than the outer disk (Krawczynski et al. 2022). Another way is by considering an outflowing Comptonizing medium (Poutanen et al. 2023; Ratheesh et al. 2023).

Our model of a parabolic, outflowing corona naturally provides a Comptonizing, outflowing “slab” at its bottom. This is shown below, where, for simplicity of the expressions, we consider an instantaneous acceleration of the outflow to speed v_0 at the bottom of it. For the full model with an acceleration region, the optical depths are calculated in Appendix A.

For a parabolic outflow, the radius of the outflow at height z is

$$R(z) = R_0(z/z_0)^{1/2}, \quad (1)$$

where R_0 is the radius at the base of the outflow, which is at height z_0 . From the continuity equation

$$2\pi R(z)^2 n_e(z) m_p v_0 = \dot{M}, \quad (2)$$

where n_e is the electron number density, m_p is the proton mass, and \dot{M} is the mass-outflow rate, one gets for the electron density

$$n_e(z) = n_0(z_0/z), \quad (3)$$

where n_0 is the density at z_0 . The Thomson optical depth $\tau_{\parallel}(z)$ from z_0 to $z > z_0$ is

$$\tau_{\parallel}(z) = \int_{z_0}^z n_e(z) \sigma_T dz = n_0 \sigma_T z_0 \ln(z/z_0), \quad (4)$$

while the *perpendicular* Thomson optical depth at height z is

$$\begin{aligned} \tau_{\perp}(z) &= n_e(z) \sigma_T R(z) = n_0(z_0/z) \sigma_T R_0(z/z_0)^{1/2} \\ &= n_0 \sigma_T R_0 (z_0/z)^{1/2}, \end{aligned} \quad (5)$$

or

$$\tau_{\perp}(z) = \frac{R_0}{z_0} \frac{(z_0/z)^{1/2}}{\ln(z/z_0)} \tau_{\parallel}(z). \quad (6)$$

The ratio of the optical depth $\tau_{\perp}(z)$ to the *total* optical depth along the outflow $\tau_{\parallel}(H) \equiv \tau_{\parallel}$ is

$$\frac{\tau_{\perp}(z)}{\tau_{\parallel}} = \frac{\ln(z/z_0)}{\ln(H/z_0)}, \quad (7)$$

which means that

$$\tau_{\perp}(z) = \frac{\ln(z/z_0)}{\ln(H/z_0)} \tau_{\parallel}. \quad (8)$$

Here H is the height of the outflow that we take it to be $H = 10^5 R_g$, where R_g is the gravitational radius.

Figure 12 shows the variation of the parallel τ_{\parallel} and the perpendicular τ_{\perp} optical depths as functions of distance z from the black hole, when an acceleration region is present (i.e., the physical case, solid lines, Appendix A) and when it is absent (i.e. the non-physical, but simpler, case of instant acceleration, dashed lines). Figure 12 implies that, at its bottom, the outflow behaves like a slab, because $\tau_{\perp} \gg \tau_{\parallel}$. In Sect. 2.8 (see also Fig. 10) we indicated that most of the scatterings occur near the bottom of the accretion flow, especially in the HS, because the optical depth is high. Thus, in the HS, the bottom of the outflow is seen by the incoming soft photons as an “outflowing slab” and therefore the X-ray polarization is expected to be along the outflow. In the HIMS, on the other hand, the outflowing corona (at least for GX 339–4) is nearly transparent ($\tau_{\parallel} \sim 1$). The soft photons travel along the outflow and scatter on average once. Thus, in the HIMS, the X-ray polarization is expected to be perpendicular to the outflow.

3. Summary and conclusion

We have demonstrated that we can reproduce most of the results from our previous works even with a non-relativistic outflow. These are: *i*) the energy spectrum (Fig. 1), *ii*) the dependence of the time-lag on Fourier frequency (Fig. 2), *iii*) the log-linear dependence of the time lag on photon energy, *iv*) the correlation between the time lag and the photon index Γ in GX 339–4 and Cyg X–1 (Fig. 5), *v*) the time-lag – cutoff-energy correlation observed in GX 339–4 (Fig. 7), and *vi*) the fact that the outflow provides a natural lamp post for the hard X-ray photons that return to the disk (Fig. 10).

The reduction of the outflow speed implies that the fraction of back-scattered photons increases and their spectrum displays about the same Γ as the photons directly escaping to the observer (unlike the models with $v_0 = 0.8c$, which produce softer spectra for the photons that return to the disk compared to those that go directly to the observer). This is because the boost in the forward direction is highly reduced. Hence the number of photons that travel at larger distances decreases. Owing to the smaller boost along the outflow axis in the case of $v_0 = 0.1c$, as compared to the case of $v_0 = 0.8c$, there is little inclination dependence of the photon index (Fig. 8), as expected. A more realistic calculation would require a parabolic outflow with a distribution of outflow velocities that decreases as one moves away from the axis. In other words, the outflow should be composed of a mildly relativistic and narrow part at its core and a less and less relativistic outflow at larger transverse distances.

As in the case of a mildly relativistic outflow ($v_0 = 0.8c$), our model with $v_0 = 0.1c$ reproduces the observations by changing only two parameters: the optical depth along the outflow axis τ_{\parallel} and the radius R_0 at its base, and these two parameters are correlated (Fig. 6), so our model has only one parameter. Our simulations in the present work ($v_0 = 0.1c$ and for GX 339–4) require a slightly smaller range in optical depth ($1 \lesssim \tau_{\parallel} \lesssim 6$) and a slightly larger range in outflow radius ($50 \lesssim R_0/R_g \lesssim 1.5 \times 10^3$) compared to the $v_0 = 0.8c$ case for which $2 \lesssim \tau_{\parallel} \lesssim 11$ and $30 \lesssim R_0/R_g \lesssim 600$. The mass-outflow rate is of the order of 1 – 5 times the Eddington rate for a 10 solar-mass black hole in the HS and 10 – 50 times the Eddington rate in the HIMS. We remark, however, that the simplifying assumption of constant outflow speed makes the numbers unreliable. Future calculations, with a realistic outflow speed as a function of radius, will address this issue properly.

Finally we note that in the HS (no matter what the outflow speed is), the bottom of the outflow, where most of the scatterings occur, is like a “slab”, which produces X-ray polarization

parallel to the outflow. In the HIMS and for GX 339–4, for which τ_{\parallel} is of order unity, we predict that the polarization will be perpendicular to the outflow.

Acknowledgements. We thank Alexandros Tsouros for offering us his code, which computes the radio emission from the outflow. We also thank an anonymous referee for a thorough reading of the manuscript, which resulted in useful comments.

References

- Altamirano, D. & Méndez, M. 2015, *MNRAS*, 449, 4027
- Arévalo, P. & Uttley, P. 2006, *MNRAS*, 367, 801
- Asada, K. & Nakamura, M. 2012, *ApJ*, 745, L28
- Bambi, C., Brenneman, L. W., Dauser, T., et al. 2020, *arXiv e-prints*, arXiv:2011.04792
- Belloni, T. M. 2010, in *Lecture Notes in Physics*, Berlin Springer Verlag, Vol. 794, *Lecture Notes in Physics*, Berlin Springer Verlag, ed. T. Belloni, 53
- Blandford, R. D. & Begelman, M. C. 1999, *MNRAS*, 303, L1
- Bright, J. S., Fender, R. P., Motta, S. E., et al. 2020, *Nature Astronomy*, 4, 697
- Cassatella, P., Uttley, P., Wilms, J., & Poutanen, J. 2012, *MNRAS*, 422, 2407
- Castro, M., D’Amico, F., Braga, J., et al. 2014, *A&A*, 569, A82
- Corbel, S., Aussel, H., Broderick, J. W., et al. 2013, *MNRAS*, 431, L107
- Corbel, S., Fender, R. P., Tzioumis, A. K., et al. 2000, *A&A*, 359, 251
- Corbel, S., Nowak, M. A., Fender, R. P., Tzioumis, A. K., & Markoff, S. 2003, *A&A*, 400, 1007
- Crary, D. J., Finger, M. H., Kouveliotou, C., et al. 1998, *ApJ*, 493, L71
- Cui, W., Zhang, S. N., Focke, W., & Swank, J. H. 1997, *ApJ*, 484, 383
- Dauser, T., García, J., Parker, M. L., Fabian, A. C., & Wilms, J. 2014, *MNRAS*, 444, L100
- Dauser, T., García, J., Walton, D. J., et al. 2016, *A&A*, 590, A76
- Dauser, T., García, J., Wilms, J., et al. 2013, *MNRAS*, 430, 1694
- Dauser, T., García, J. A., Joyce, A., et al. 2022, *MNRAS*, 514, 3965
- Dexter, J. & Quataert, E. 2012, *MNRAS*, 426, L71
- Di Matteo, T. & Psaltis, D. 1999, *ApJ*, 526, L101
- Done, C., Gierliński, M., & Kubota, A. 2007, *A&A Rev.*, 15, 1
- Espinasse, M. & Fender, R. 2018, *MNRAS*, 473, 4122
- Gallo, E., Fender, R. P., & Pooley, G. G. 2003, *MNRAS*, 344, 60
- Gallo, E., Miller, B. P., & Fender, R. 2012, *MNRAS*, 423, 590
- Giannios, D. 2005, *A&A*, 437, 1007
- Giannios, D., Kylafis, N. D., & Psaltis, D. 2004, *A&A*, 425, 163
- Grinberg, V., Pottschmidt, K., Böck, M., et al. 2014, *A&A*, 565, A1
- Hannikainen, D. C., Hunstead, R. W., Campbell-Wilson, D., & Sood, R. K. 1998, *A&A*, 337, 460
- Ingram, A., Bollemeijer, N., Veledina, A., et al. 2023, *arXiv e-prints*, arXiv:2311.05497
- Kalamkar, M., Reynolds, M. T., van der Klis, M., Altamirano, D., & Miller, J. M. 2015, *ApJ*, 802, 23
- Kalemci, E., Tomsick, J. A., Buxton, M. M., et al. 2005, *ApJ*, 622, 508
- Kalemci, E., Tomsick, J. A., Rothschild, R. E., et al. 2003, *ApJ*, 586, 419
- Kara, E., Steiner, J. F., Fabian, A. C., et al. 2019, *Nature*, 565, 198
- Karpouzas, K., Méndez, M., García, F., et al. 2021, *MNRAS*, 503, 5522
- Kotov, O., Churazov, E., & Gilfanov, M. 2001, *MNRAS*, 327, 799
- Kovalev, Y. Y., Pushkarev, A. B., Nokhrina, E. E., et al. 2020, *MNRAS*, 495, 3576
- Krawczynski, H., Muleri, F., Dovčiak, M., et al. 2022, *Science*, 378, 650
- Kroon, J. J. & Becker, P. A. 2016, *ApJ*, 821, 77
- Kylafis, N. D., Papadakis, I. E., Reig, P., Giannios, D., & Pooley, G. G. 2008, *A&A*, 489, 481
- Kylafis, N. D. & Reig, P. 2018, *A&A*, 614, L5
- Kylafis, N. D., Reig, P., & Papadakis, I. 2020, *A&A*, 640, L16
- Kylafis, N. D., Reig, P., & Tsouros, A. 2023, *A&A*, 679, A81
- Lyubarskii, Y. E. 1997, *MNRAS*, 292, 679
- Markoff, S., Falcke, H., & Fender, R. 2001, *A&A*, 372, L25
- McClintock, J. E. & Remillard, R. A. 2006, *Black hole binaries*, ed. W. H. G. Lewin & M. van der Klis, 157–213
- Méndez, M., Karpouzas, K., García, F., et al. 2022, *Nature Astronomy*, 6, 577
- Merloni, A., Fabian, A. C., & Ross, R. R. 2000, *MNRAS*, 313, 193
- Mitsuda, K., Inoue, H., Koyama, K., et al. 1984, *PASJ*, 36, 741
- Miyamoto, S., Kitamoto, S., Mitsuda, K., & Dotani, T. 1988, *Nature*, 336, 450
- Motta, S., Belloni, T., & Homan, J. 2009, *MNRAS*, 400, 1603
- Motta, S. E., Casella, P., & Fender, R. P. 2018, *MNRAS*, 478, 5159
- Nowak, M. A., Dove, J. B., Vaughan, B. A., Wilms, J., & Begelman, M. C. 1999a, *Nuclear Physics B Proceedings Supplements*, 69, 302
- Nowak, M. A., Vaughan, B. A., Wilms, J., Dove, J. B., & Begelman, M. C. 1999b, *ApJ*, 510, 874
- Pottschmidt, K., Wilms, J., Nowak, M. A., et al. 2003, *A&A*, 407, 1039
- Poutanen, J. 2001, *Advances in Space Research*, 28, 267
- Poutanen, J. & Fabian, A. C. 1999, *MNRAS*, 306, L31
- Poutanen, J., Nagendra, K. N., & Svensson, R. 1996, *MNRAS*, 283, 892
- Poutanen, J., Veledina, A., & Beloborodov, A. M. 2023, *ApJ*, 949, L10
- Ratheesh, A., Rankin, J., Costa, E., et al. 2023, *Journal of Astronomical Telescopes, Instruments, and Systems*, 9, 038002
- Reig, P. & Kylafis, N. D. 2015, *A&A*, 584, A109
- Reig, P. & Kylafis, N. D. 2019, *A&A*, 625, A90
- Reig, P. & Kylafis, N. D. 2021, *A&A*, 646, A112
- Reig, P., Kylafis, N. D., & Giannios, D. 2003, *A&A*, 403, L15
- Reig, P., Kylafis, N. D., Papadakis, I. E., & Costado, M. T. 2018, *MNRAS*, 473, 4644
- Remillard, R. A. & McClintock, J. E. 2006, *ARA&A*, 44, 49
- Rodríguez Cavero, N., Marra, L., Krawczynski, H., et al. 2023, *ApJ*, 958, L8
- Rybicki, G. B. & Lightman, A. P. 1979, *Radiative processes in astrophysics*
- Schnittman, J. D. & Krolik, J. H. 2010, *ApJ*, 712, 908
- Shakura, N. I. & Sunyaev, R. A. 1973, *A&A*, 24, 337
- Shaposhnikov, N. & Titarchuk, L. 2009, *ApJ*, 699, 453
- Shaw, A. W., Plotkin, R. M., Miller-Jones, J. C. A., et al. 2021, *ApJ*, 907, 34
- Shidatsu, M., Ueda, Y., Yamada, S., et al. 2014, *ApJ*, 789, 100
- Stevens, A. L. & Uttley, P. 2016, *MNRAS*, 460, 2796
- Stiele, H., Belloni, T. M., Kalemci, E., & Motta, S. 2013, *MNRAS*, 429, 2655
- Sunyaev, R. A. & Truemper, J. 1979, *Nature*, 279, 506
- Uttley, P., Cackett, E. M., Fabian, A. C., Kara, E., & Wilkins, D. R. 2014, *A&A Rev.*, 22, 72
- Uttley, P. & Malzac, J. 2023, *arXiv e-prints*, arXiv:2312.08302
- Uttley, P., Wilkinson, T., Cassatella, P., et al. 2011, *MNRAS*, 414, L60
- Vaughan, B. A. & Nowak, M. A. 1997, *ApJ*, 474, L43
- Veledina, A., Muleri, F., Dovčiak, M., et al. 2023, *ApJ*, 958, L16
- Weisskopf, M. C., Soffitta, P., Baldini, L., et al. 2022, *Journal of Astronomical Telescopes, Instruments, and Systems*, 8, 026002

Appendix A: Description of the model

Appendix A.1: Introduction

Our model simulates with Monte Carlo the process of Comptonization in an outflow of matter, ejected in BHBs from the hot inner flow in the vicinity of the black hole, perpendicular to the accretion disk. Because the Bernoulli integral of the hot inner flow is positive (Blandford & Begelman 1999), the matter cannot fall into the black hole, hence part of the hot inner flow must escape as an outflow. In other words, the hot inner flow is not just a static corona rotating around the black hole, but a wind-like, “outflowing corona”. The thin accretion disk in the accretion flow is the source of blackbody photons at the base of the outflow. These soft photons either escape unscattered or are scattered in the outflow and have their energy increased, on average. This upscattering of the soft blackbody photons produces the hard X-ray power law. Furthermore, the same upscattering causes an average time lag of the harder photons with respect to the softer ones.

Appendix A.2: Morphology

Observational studies of the collimation of jets in active galactic nuclei (AGN) have shown that a large fraction of near-by AGN start with a parabolic outflow, which changes to a conical one further out (Asada & Nakamura 2012; Kovalev et al. 2020). Invoking the morphological similarity between AGN and BHBs, we assume that the outflow in BHBs has a parabolic form or something close to it. Therefore, we model the radius of the outflow, as a function of height z from the black hole, as

$$R(z) = R_0 (z/z_0)^\beta, \quad (\text{A.1})$$

where R_0 is the radius of the outflow at its base, which is taken to be at a distance z_0 from the black hole. We take the index β to be $1/2$, though values close to it do not produce different results.

Appendix A.3: Outflow acceleration

At the bottom of the outflow, there must be an acceleration region ($z_0 \leq z \leq z_1$), beyond which the flow speed is constant and equal to v_0 . Thus, the speed of the outflowing matter along the z axis is taken to be

$$v_{\parallel}(z) = \begin{cases} v_0 (z/z_1)^a, & z_0 \leq z \leq z_1 \\ v_0, & z > z_1, \end{cases} \quad (\text{A.2})$$

where we take $a = 1/2$, though its exact values is not crucial.

Appendix A.4: Optical depths

If $n_e(z)$ is the number density of electrons along the outflow, mass conservation requires that

$$\dot{M} = 2\pi R^2(z) m_p n_e(z) v_{\parallel}(z), \quad (\text{A.3})$$

where the factor 2 is for both sides of the outflow, \dot{M} is the total mass-outflow rate, and m_p is the proton mass. The outflowing matter is considered to be consisting of protons and electrons only. Eqs. (A.1, A.2, and A.3) imply that the number density of electrons along the outflow is given by

$$n(z) = \begin{cases} n_1 (z_1/z)^{a+1}, & z_0 \leq z \leq z_1 \\ n_1 (z_1/z), & z > z_1, \end{cases} \quad (\text{A.4})$$

where n_1 is the number density of electrons at z_1 , while the density at the base of the outflow is $n_0 = n_1(z_1/z_0)^{a+1}$.

The Thomson optical depth of the outflow along z is given by

$$\tau_{\parallel} = \int_{z_0}^H n_e(z) \sigma_T dz \quad (\text{A.5})$$

where σ_T is the Thomson cross section and H is the height of the outflow. Using Eq. (A.4) we find

$$\tau_{\parallel} = \frac{n_1 \sigma_T z_1}{a} [(z_1/z_0)^a - 1] + n_1 \sigma_T z_1 \ln(H/z_1). \quad (\text{A.6})$$

Instead of n_0 , we take τ_{\parallel} as a model parameter. Thus, our two main parameters are τ_{\parallel} and R_0 .

The Thomson optical depth $\tau_{\parallel}(z)$ from z_0 to z , $z_0 < z < H$ is

$$\tau_{\parallel}(z) = \int_{z_0}^z n_e(z) \sigma_T dz \quad (\text{A.7})$$

or

$$\tau_{\parallel}(z) = \begin{cases} \frac{n_1 \sigma_T z_1}{a} \left[\left(\frac{z_1}{z_0} \right)^a - \left(\frac{z_1}{z} \right)^a \right], & z_0 \leq z \leq z_1 \\ \frac{n_1 \sigma_T z_1}{a} \left[\left(\frac{z_1}{z_0} \right)^a - 1 \right] + n_1 \sigma_T z_1 \ln(z/z_1), & z > z_1 \end{cases} \quad (\text{A.8})$$

while the perpendicular Thomson optical depth at height z is

$$\tau_{\perp}(z) = n_e(z) \sigma_T R(z) = \begin{cases} n_1 \left(\frac{z_1}{z} \right)^{a+1} \sigma_T R_0 \left(\frac{z}{z_0} \right)^p, & z_0 \leq z \leq z_1 \\ n_1 \left(\frac{z_1}{z} \right) \sigma_T R_0 \left(\frac{z}{z_0} \right)^p, & z > z_1. \end{cases} \quad (\text{A.9})$$

Appendix A.5: Magnetic field

For computational simplicity, we assume the magnetic field in the outflow to be along the axis of the outflow, the z axis. The z -dependence of the magnetic field is dictated by magnetic flux conservation to be

$$B(z) = B_0(z_0/z), \quad (\text{A.10})$$

where B_0 is the magnetic field strength at the base of the outflow.

Appendix A.6: Lorentz factor

The electrons are assumed to move on helical orbits around the magnetic field, with velocity components $v_{\parallel}(z)$ and v_{\perp} . Their Lorentz factor is

$$\gamma(z) = 1 / \sqrt{1 - [v_{\parallel}(z)^2 + v_{\perp}^2] / c^2}, \quad (\text{A.11})$$

where $v_{\parallel}(z)$ is given by Eq. (A.2). In the coasting region of the outflow ($z > z_1$), the Lorentz factor of the electrons is

Table A.1. Parameters of the model

Symbol	Value	Units	Parameter
β	0.5^a	–	Index of the radial dependence with height of the outflow
τ_{\parallel}	1 – 6	–	Optical depth to electron scattering along the axis of the outflow
R_0	50 – 1500	R_g^b	Radius of the outflow at its base
γ_0^c	1.10–1.15	–	Lorentz factor of the electrons, when the flow is coasting
kT_{BB}	0.2	keV	Characteristic energy of the input soft photons
z_0	5	R_g	Distance of the bottom of the outflow from the black hole
H	10^5	R_g	Height of the outflow
z_1	50	R_g	Height of the acceleration zone
a	0.5	–	Exponent of the velocity profile in the acceleration zone
R_{disk}	10^3	R_{ISCO}^d	Outer radius of the accretion disk
$\cos \theta^e$	–1 to 1	–	θ is the viewing angle
m	10	M_{\odot}	Mass of the black hole
N_{phot}	$10^7 - 10^8$	–	Number of simulated photon beams
p^f	3	–	Index of the Lorentz factor power-law distribution
γ_{min}^f	1	–	Lower limit of the Lorentz factor power-law distribution
γ_{max}^f	500	–	Upper limit of the Lorentz factor power-law distribution

Notes.

^a: $\beta = 0.5$ assumes a parabolic outflow

^b: Gravitational radius $R_g = Gm/c^2$. $R_g \approx 1.48 \times 10^6$ cm for a $m = 10 M_{\odot}$ black hole

^c: $\gamma_0 = 1/\sqrt{1 - (v_0^2 + v_{\perp}^2)/c^2}$

^d: Radius of the inner-most stable circular orbit.

^e: θ is the angle between the observer and the outflow axis. The code records the escaping direction of the photon in bins of 0.1 in $w = \cos \theta$, from $w = -1$ to $w = 1$. Negative values indicate back scattering.

^f: For the computation of the radio emission.

$$\gamma_0 = 1/\sqrt{1 - [v_0^2 + v_{\perp}^2]/c^2}. \quad (\text{A.12})$$

It has been verified (Giannios 2005) that a power law distribution of electron velocities in the rest frame of the flow (see next subsection) gives nearly identical results. This is because the dominant contribution to the scatterings comes from the electrons that have the lowest velocity (or the lowest Lorentz γ factor), due to the steep power law of electron γ 's distribution required to explain the overall spectrum.

Appendix A.7: Radio spectrum

For the computation of the radio spectrum produced by the outflow, the full distribution of electron speeds or Lorentz γ must be taken into account.

In the rest frame of the flow, the electrons are generally taken to have a power-law distribution of Lorentz γ , namely

$$N_e(\gamma_{\text{co}}) = N_0 \gamma_{\text{co}}^{-p}, \quad (\text{A.13})$$

from γ_{min} to γ_{max} , where p , γ_{min} , and γ_{max} are parameters of the model. Here, γ_{co} is the Lorentz factor of the electrons in the co-moving frame.

In order to calculate the distribution of the electrons for an observer at rest, one would need to perform the transformation of the Lorentz factor from γ_{co} to γ . If one assumes that the velocity of the outflow is constant throughout, then it can be shown that γ is approximately proportional to γ_{co} , and thus Eq. (A.13) also holds for an observer at rest. Since the acceleration region is small, the contribution of the acceleration region to the radio

emission of the outflow is small. Thus, we neglect the transformation from γ_{co} to γ and take the distribution of electrons for the observer at rest to be

$$N_e(\gamma) \simeq N_0 \gamma^{-p}. \quad (\text{A.14})$$

The normalization $N_0(z)$ can be calculated by integrating Eq. (A.14) from γ_{min} to γ_{max} , and equating the expression with the co-moving electron density. This yields

$$N_0(z) = n(z) \sqrt{1 - \frac{v_{\parallel}^2(z)}{c^2}} (p-1) \gamma_{\text{min}}^{p-1}. \quad (\text{A.15})$$

Ignoring synchrotron self-Compton (for a justification see Giannios 2005), the equation for the transfer of radio photons in the outflow, in direction \hat{n} , along which length is measured by s , is given by

$$\frac{dI(\nu, s)}{ds} = j(\nu, s) - a(\nu, s)I(\nu, s), \quad (\text{A.16})$$

where $j(\nu, s)$ and $a(\nu, s)$ are the emission and absorption coefficients respectively, and $I(\nu, s)$ is the intensity at frequency ν at position s . The formal solution of this equation is

$$I_{\nu} = \int_{s_1}^{s_2} ds j(\nu, s) \exp\left(-\int_s^{s_2} ds' a(\nu, s')\right). \quad (\text{A.17})$$

For \hat{n} perpendicular to the outflow axis, this is simplified to

$$I_{\nu}(z) = \frac{j(\nu, z)}{a(\nu, z)} [1 - \exp\{-a(\nu, z)R(z)\}], \quad (\text{A.18})$$

where $R(z)$ is given by Eq. (A.1), since the emission and absorption coefficients depend only on z . The total power radiated per unit frequency per unit solid angle is thus given by

$$\frac{dE_\nu}{dt d\nu d\Omega} = 2\pi \int_{z_0}^H dz I_\nu(z) R(z). \quad (\text{A.19})$$

Now, we need to specify the absorption and emission coefficients. Since the radio emission of the outflow is due to synchrotron emitting electrons, whose Lorentz factors follow a power law as in Eq. (A.14), the absorption and emission coefficients can be calculated analytically (Rybicki & Lightman 1979). The expressions are

$$a(\nu, z) = \frac{\sqrt{3}q^3}{8\pi m_e} \left(\frac{3q}{2\pi m_e^3 c^5} \right)^{\frac{p}{2}} N_0(z) B^{\frac{p+2}{2}}(z) \times \Gamma\left(\frac{p}{4} + \frac{1}{6}\right) \Gamma\left(\frac{3p+22}{12}\right) (m_e c^2)^{p-1} \nu^{-\frac{p+4}{2}}, \quad (\text{A.20})$$

and

$$j(\nu, z) = \frac{\sqrt{3}q^3 N_0(z) B(z)}{4\pi m_e c^2 (p+1)} \times \Gamma\left(\frac{p}{4} + \frac{19}{12}\right) \Gamma\left(\frac{p}{4} - \frac{1}{12}\right) \left(\frac{2\pi m_e c^2}{3qB(z)}\right)^{\frac{1-p}{2}} \nu^{\frac{1-p}{2}}, \quad (\text{A.21})$$

where q and m_e are the absolute value of the charge and the mass, respectively, of the electron, $B(z) = B_0(z_0/z)$ is the strength of the magnetic field at height z assuming flux freezing, $B_0 = B(z_0)$, and Γ is the Gamma-function.

Integrating Eq. (A.19) over solid angles, gives the power per unit frequency radiated,

$$P(\nu) \equiv \frac{dE_\nu}{dt d\nu} = 4\pi^2 \int_{z_0}^H dz I_\nu(z) R(z). \quad (\text{A.22})$$

Since there are two outflows with opposite directions to each other, an observer at a distance d , whose line of sight makes a 90-degree angle with the outflow axis, will measure a flux of

$$F(\nu) = \frac{2P(\nu)}{4\pi d^2}, \quad (\text{A.23})$$

where d is the distance to the source. Since the observer's line of sight is taken to be perpendicular to the outflow axis, there is no need to account for a Doppler shift.

Appendix A.8: Parameters of the model

The main parameters of the model are the optical depth τ_{\parallel} (see Eq. A.6) and the width of the outflow at its base R_0 (see Eq. A.1). Another parameter that we occasionally vary is the Lorentz factor γ_0 (see Eq. A.11). These are the only parameters that we vary to obtain our results. The ranges of variation of these parameters are shown in Table A.1. The physical reason behind the importance of these three parameters is the following: a variation in optical depth is equivalent to a change in the density at the base of the outflow. The denser the medium, the more scatterings are expected and more energetic photons will escape. Hence, τ_{\parallel} is the prime parameter that drives the changes in the photon index

Γ . A change in R_0 corresponds to a change in the size of the jet. The larger the medium, the longer distances the photons travel. Hence time lags are strongly affected by changes in R_0 . Finally, an increase in v_{\perp} (or γ_0) mimics the increase of the temperature in the case of thermal Comptonization.

The index β (see Eq. A.1) is also an important parameter because it defines the morphology of the outflow. However, in this case we fix it to 1/2, which means that the shape of the outflow is parabolic.

The rest of the parameters of the model are the blackbody temperature kT_{BB} of the soft input spectrum from the accretion disk that enters at the bottom of the outflow, the height z_0 from the black hole of the bottom of the outflow, the total height H from the black hole of the outflow, the height z_1 from the black hole at which the acceleration of the outflow stops, the exponent a of the velocity profile in the acceleration region (see Eq. A.2), the outer radius R_{disk} of the Shakura-Sunyaev accretion disk, the mass m of the black hole in solar-mass units, the number N_{phot} of simulated photon beams by the Monte Carlo code, and the exponent p of the distribution of electron Lorentz factors (see Eq. A.13), along with the limits γ_{min} and γ_{max} . None of these parameters is crucial and their values are shown in Table A.1.

To have good statistics in our Monte Carlo results, we combined all the escaping photons with directional cosine with respect to the axis of the outflow in a given range $\cos \theta_{\text{min}} \leq \cos \theta < \cos \theta_{\text{max}}$.

Appendix A.9: How the code works

Photons from the inner part of the accretion disk, in the form of a blackbody distribution of characteristic temperature T_{BB} , are injected at the base of the outflow with an upward isotropic distribution. Each photon is given a weight equal to unity (equivalently, it can be viewed as a beam of flux unity) when it leaves the accretion disk, and its time of flight is set equal to zero. The optical depth $\tau(\hat{n})$ along the photon's direction \hat{n} is computed from the position where the photon started or scattered to the boundary of the outflow and a fraction $e^{-\tau(\hat{n})}$ of the photon's weight escapes and is recorded. The rest of the weight of the photon gets scattered in the outflow. If the effective optical depth in the outflow is significant (i.e., $\gtrsim 1$), then a progressively smaller and smaller weight of the photon experiences more and more scatterings. When the remaining weight in a photon becomes less than a small number (typically 10^{-8}), we start with a new photon.

The time of flight of a random walking photon (or more accurately of its remaining weight) gets updated at every scattering by adding the last distance traveled divided by the speed of light. For the escaping weight along a travel direction we add an extra time of flight *outside* the comptonizing region in order to bring in step all the photons (or better the fractions of them) that escape in a given direction from different points of the boundary of the outflow. The more a fractional photon stays in the comptonizing region, the more energy it gains, on average, mainly from the circular motion (i.e., v_{\perp}) of the electrons. Such Comptonization can occur everywhere in the outflow. Yet, a photon that random walks high up in the outflow has a larger time of flight than a photon that random walks near the bottom of the outflow. The optical depth to electron scattering $\tau(\hat{n})$, the energy shift, and the new direction of the photons after scattering are computed using the corresponding relativistic expressions.

Since the defining parameters of a photon (position, direction, energy, weight, and time of flight) at each stage of its flight are computed, then we can determine not only the spectrum of the radiation emerging from the scattering medium and the time

of flight of each escaping fractional photon, but also the distribution of escaping heights from the outflow and the distribution of directions of escape. To have good statistics in our Monte Carlo results, we combine all the escaping photons with directional cosine within a given range.

The time of flight of all escaping fractional photons is recorded in N_{bin} time bins of duration δt s each. In this way, we can compute the number of photons that are emitted from the outflow in each time bin, and for any energy band. In other words, we can create $N_{\text{bin}} \times \delta t$ s long light curves, for any energy band, which correspond to the resulting emission of the outflow in response to an instantaneous burst of soft photons which we assume enter the outflow simultaneously. Having created light curves in various energy bands, we can now compute delays between any pair of bands. Following Vaughan & Nowak (1997), we compute the phase lag and through it the time lag between the two energy bands as a function of Fourier frequency $\tau(\nu) = \phi/2\pi\nu$. Then we compute the average time lag, $\langle t_{\text{lag}} \rangle$, in a given Fourier frequency range³.

The outflow velocity boosts the photons in the forward direction. Naturally, this effect is stronger as the outflow speed v_{\parallel} increases. Regardless of the value of v_{\parallel} (or γ if one includes v_{\perp}), a fraction of photons are back scattered. The fraction of back scattered photons decreases as v_{\parallel} increases. We distinguish the photons that hit the accretion disk after escape and those that do not. In this way, we can compute the reflection fraction as the number of photons that irradiate ("hit") the disk over the number of photons that escape in the direction of the observer. By dividing the accretion disk into radial zones, we can also compute the emissivity index q , which is the index of the power law $F(r) \propto r^{-q}$ of the radially dependent flux irradiating the disk by the outflow.

³ Typically, $N_{\text{bin}} = 8192$, $\delta t = 1/64$ s. The energy bands are taken to match the data results that we want to reproduce. The same applies to the frequency range where the average lags are computed.